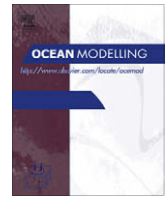




Contents lists available at ScienceDirect

Ocean Modelling

journal homepage: www.elsevier.com/locate/ocemod

A spectral barotropic model of the wind-driven world ocean

Thomas Frisius^{a,b,*}, Klaus Fraedrich^{a,b}, Xiuhua Zhu^b, Weiqiang Wang^c^a Meteorologisches Institut, KlimaCampus, Universität Hamburg, Germany^b Max Planck Institute for Meteorology, KlimaCampus, Hamburg, Germany^c Institut für Meereskunde, KlimaCampus, Universität Hamburg, Germany

ARTICLE INFO

Article history:

Received 26 January 2009

Received in revised form 27 July 2009

Accepted 28 July 2009

Available online 12 August 2009

Keywords:

Depth-averaged flow

Spectral model

Implicit modelling

Wind-driven ocean circulation

Ocean wave-dynamics

ABSTRACT

A global spectral barotropic ocean model is introduced to describe the depth-averaged flow. The equations are based on vorticity and divergence (instead of horizontal momentum); continents exert a nearly infinite drag on the fluid. The coding follows that of spectral atmospheric general circulation models using triangular truncation and implicit time integration to provide a first step for seamless coupling to spectral atmospheric global circulation models and an efficient method for filtering of ocean wave dynamics. Five experiments demonstrate the model performance: (i) Bounded by an idealized basin geometry and driven by a zonally uniform wind stress, the ocean circulation shows close similarity with Munk's analytical solution. (ii) With a real land–sea mask the model is capable of reproducing the spin-up, location and magnitudes of depth-averaged barotropic ocean currents. (iii) The ocean wave-dynamics of equatorial waves, excited by a height perturbation at the equator, shows wave dispersion and reflection at eastern and western coastal boundaries. (iv) The model reproduces propagation times of observed surface gravity waves in the Pacific with real bathymetry. (v) Advection of tracers can be simulated reasonably by the spectral method or a semi-Lagrangian transport scheme. This spectral barotropic model may serve as a first step towards an intermediate complexity spectral atmosphere–ocean model for studying atmosphere–ocean interactions in idealized setups and long term climate variability beyond millennia.

© 2009 Elsevier Ltd. All rights reserved.

1. Introduction

A numerically efficient spectral solution technique for hydrostatic atmospheric equations on the sphere has been developed in the seventies (Bourke, 1972; Bourke, 1974; Hoskins and Simmons, 1975). This forms the basis of many atmospheric global circulation models (AGCMs) that are in use in the scientific community for weather forecasting and climate modelling (e.g. Kalnay et al., 1990; Kiehl et al., 1996). The main advantages of the spectral solution technique lie in the absence of numerical problems due to the singularities at the poles, a better representation of wave dynamics, and the simple way of spatial differentiation that allows the inversion of many linear differential operators without much effort. However, this technique has never been applied to the modelling of the real global ocean circulation, which often employs finite-difference approaches (see, e.g. Haidvogel and Beckmann, 1999). The reason seems obvious since, contrary to the atmosphere, the ocean is bounded by coast lines where at least the normal flow must vanish identically. Neverthe-

less, spectral models have been successfully applied to the simulation of the ocean circulation in idealized rectangular basins using trigonometric functions (e.g. Böning, 1986) or using Chebishev polynomials (e.g. Haidvogel et al., 1980).

In this study we present a method by which the flow around the continents can be reasonably simulated with a spectral solution technique. This builds on the method of Mason and Sykes (1978) who considered atmospheric flows over mountains. They viewed the mountain as a part of the fluid having an infinitely large viscosity. This enables inclusion of arbitrarily shaped mountains in a model with a regular grid in a Cartesian coordinate system. Furthermore, the diagnostic Poisson equation for pressure can be solved without paying attention to complicated boundary conditions due to orography. The treatment of boundaries in this way has been successfully applied in a large-eddy simulation (LES) model for simulating the flow above complex terrain (Reinert et al., 2007). In principle this method can also be applied to modelling of the world ocean where the bathymetry and continents have a complex structure.

A spectral ocean model would have several advantages. With a spectral model a flow over or near the pole can be simulated without additional care taken of the singularity of the longitude–latitude coordinates. Furthermore, a spectral ocean model allows a seamless coupling to spectral AGCMs since, in both models, fields

* Corresponding author. Present address: Meteorologisches Institut, KlimaCampus, Universität Hamburg, Grindelberg 5, 20144 Hamburg, Germany. Tel.: +49 40428385068.

E-mail address: Thomas.Frisius@zmaw.de (T. Frisius).

are transformed to a Gaussian grid that can be identical. Another advantage is the more efficient inversion of linear operators, because the number of grid-points representing a field with a certain resolution is about a factor 4.5 larger than the corresponding number of spectral functions, namely the spherical harmonics. Furthermore, the application of many linear differential operators on spherical harmonics can be expressed by simple recurrence relations. For example, the inversion of the Laplace operator is extraordinarily simple, because spherical harmonics are eigenfunctions while, in a grid-point model, a much more complicated iterative elliptic solver has to be used.

For climate modelling the main interest lies in the large scale ocean circulation, for which the Rossby number is very small. In such a case it is reasonable to neglect advection in the momentum equation. This leads to governing equations having nonlinearities only in the thermodynamic and salinity equations. For some purposes it is of interest to determine the steady state circulation for fixed temperature, salinity, and wind stress fields in a filtered model, where the ocean is assumed to be geostrophically adjusted due to slow changes in temperature, salinity and wind stress. In such a model ocean wave dynamics is filtered out and all variability is due to advection of temperature and salinity as well as external forcing. This sets a linear problem that can be solved more efficiently in spectral space due to the aforementioned reasons. Such a model has been suggested by Hasselmann (1982) to be valid for the purpose of simulating climate variability. Indeed, the Large Scale Geostrophic (LSG) model (Maier-Reimer et al., 1993) is primarily based on these ideas and has been successfully applied in climate modelling (e.g. Cubasch et al., 1992; von Storch et al., 1997). Modeling results by Te Raa and Dijkstra (2002) indicate that ocean wave dynamics is unimportant for the variability of the thermohaline ocean circulation on interdecadal timescales in their idealized basin experiments which exclude the possibly important impact of tides (e.g. Wunsch and Ferrari, 2004). However, the effect of ocean wave dynamics filtering has not been investigated so far. Neelin (1991) also suggests filtering of ocean wave dynamics; i.e. such that only advection to be relevant for the theoretical understanding of the El Niño Southern Oscillation phenomenon.

The present paper introduces a spectral model for the depth-averaged flow in the world ocean. Due to the model's simplicity this study should rather be considered as a proof of concept than an introduction of an ocean model that is already suitable for climate modelling. Our main motivation is to develop an intermediate complexity ocean circulation model which can be adopted to study (i) the effect of filtering ocean wave dynamics, (ii) ocean-atmosphere interactions in idealized model configurations and (iii) long term climate variability on time scales beyond millennia. The model presented in this study will be referred to as SOM (abbreviation for spectral ocean model). This article is organized as follows. Section 2 introduces the governing equations of SOM and describes how continents are treated in the model. In Section 3 the spectral representation of the governing equation with respect to the spherical harmonics is outlined. Section 4 describes the procedure to determine steady state solutions for a given wind forcing by the solution of the linear inhomogeneous differential equations. Section 5 presents steady and time varying solutions for idealized and realistic model configurations followed by the conclusion with an outlook (Section 6).

2. The governing equations

We assume that the ocean has uniform density and the Reynolds number (based on the horizontal eddy momentum exchange coefficient) is small. Furthermore, at mean sea level ($z = 0$), the simplified boundary condition for vertical velocity

$$w|_{z=0} = \frac{\partial h}{\partial t} \quad (1)$$

is implied where h is the displacement of the sea surface which is supposed to be very small compared to the depth H of the ocean. With these assumptions the shallow water equations without momentum advection form the governing equations for the depth-averaged wind-driven flow. They are given in nondimensional form by

$$\frac{\partial \mathbf{v}}{\partial t} + 2\mu \mathbf{k} \times \mathbf{v} = -\frac{1}{Fr^2} \nabla h + A_M \nabla^2 \mathbf{v} + \frac{\boldsymbol{\tau}}{H} + \mathbf{F}, \quad (2)$$

$$\frac{\partial h}{\partial t} = -\nabla \cdot (H\mathbf{v}), \quad (3)$$

where \mathbf{v} is the depth-averaged (from $z = 0$ to $z = -H$) horizontal velocity, Fr the Froude number, μ the sine of latitude, \mathbf{k} the unit vector in vertical direction, ∇ the Nabla operator, A_M the horizontal eddy momentum exchange coefficient, and $\boldsymbol{\tau}$ the wind stress vector. \mathbf{F} symbolizes a forcing that will be explained later. The time t has been nondimensionalized with the timescale Ω^{-1} where Ω is the angular velocity of the planet rotation. The length scale is the planet radius a , the velocity scale is Ωa , and the height scale is the mean depth H_0 . With these scales the Froude number becomes

$$Fr = \frac{\Omega a}{\sqrt{gH_0}}, \quad (4)$$

where g denotes the gravity acceleration. For $H = 1$ the model can also be interpreted as a reduced gravity model that simulates the dynamics of a uniform density layer above a deep ocean at rest with a higher density. In this case h is the downward displacement of the interface between the two layers. In a reduced gravity model, however, the Froude number is very large and one has to take care that the assumption $h \ll H$ might break down. Nevertheless, we apply the SOM in this configuration to test its ability to reproduce the dynamics of trapped equatorial waves.

For the spectral representation it is common to use vorticity and divergence equations instead of the horizontal momentum equation. After applying curl and divergence to Eq. (1) we get

$$\begin{aligned} \frac{\partial \zeta}{\partial t} = & -2\mu D - 2V + A_M (\nabla^2 \zeta + 2\zeta) - \nabla \cdot (\mathbf{k} \times \frac{\boldsymbol{\tau}}{H}) \\ & - \nabla \cdot (\mathbf{k} \times \mathbf{F}), \end{aligned} \quad (5)$$

$$\frac{\partial D}{\partial t} = 2\mu \zeta - 2U - \frac{1}{Fr^2} \nabla^2 h + A_M \nabla^2 D + \nabla \cdot (\frac{\boldsymbol{\tau}}{H}) + \nabla \cdot \mathbf{F}, \quad (6)$$

where ζ is the vertical component of the vorticity vector, D the divergence of the horizontal flow, and $(U, V) = \sqrt{1 - \mu^2}(u, v)$ the horizontal velocity weighted with the cosine of latitude. Due to Helmholtz's theorem the velocity vector \mathbf{v} can be deduced from streamfunction ψ and velocity potential χ as follows:

$$\mathbf{v} = -\nabla \times (\psi \mathbf{k}) + \nabla \chi, \quad (7)$$

which are related to vorticity and divergence, respectively, via Poisson equations

$$\zeta = \nabla^2 \psi, D = \nabla^2 \chi. \quad (8)$$

Since the equations will be solved on the complete sphere with a spectral technique no boundary conditions can be incorporated at the coast lines. In fact, fluid also exists over continents, but the land exerts a drag as large as possible so that, practically, the flow remains zero over the continents. This can be realized by setting

$$\mathbf{F} = -\delta_{LS} \frac{\mathbf{v}}{\tau_c}, \quad (9)$$

where δ_{LS} is the land-sea mask function which becomes $\delta_{LS} = 1$ over land areas and $\delta_{LS} = 0$ over oceanic areas. In order to obtain finite vorticity tendencies, the land-sea mask function can increase

continuously from zero to one in a thin transition zone at the coast lines. In this manner, a large drag is introduced over continents by damping the flow with a continental friction time scale τ_c that should be much smaller than one time-step length. One may consider the force (9) as a bottom friction force that becomes large near the coast lines and infinite over the continents due to the vanishing fluid depth. The force given in (9) is referred to as the continental drag.

3. Spectral representation

The model fields are projected onto a new base, namely the spherical harmonics. Therefore, a scalar field function $F(\lambda, \mu, t)$ is represented by

$$F(\lambda, \mu, t) = \sum_{n=0}^{\infty} \sum_{m=-n}^n F_n^m(t) Y_n^m(\lambda, \mu) e^{im\lambda}, \quad (10)$$

where Y_n^m and F_n^m denote the spherical harmonic function and the complex-valued spectral coefficient, respectively, for total wavenumber n and zonal wavenumber m (see, e.g., Platzman, 1962). Note that F becomes real when $F_n^{-m} = F_n^{m*}$. Inserting the expansion (10) for ζ , D , h , U , V , ψ , χ , τ_λ and τ_ϕ into the governing equations and applying the scalar product

$$\langle Y_n^m | \dots \rangle \equiv \frac{1}{4\pi} \int_{-1}^1 \int_0^{2\pi} Y_n^{m*}(\lambda, \mu) \dots d\lambda d\mu$$

we get, due to the orthogonality of the spherical harmonics, the following set of spectral equations

$$\begin{aligned} \frac{d\zeta_n^m}{dt} = & -2d_{m,n}D_{n-1}^m - 2d_{m,n+1}D_{n+1}^m - 2V_n^m + C_{\tau n}^m - A_M(n(n+1)-2)\zeta_n^m \\ & - \frac{1}{\tau_c} \left\langle Y_n^m \left| im \frac{V\delta_{LS}}{1-\mu^2} \right. \right\rangle + \frac{1}{\tau_c} \left\langle Y_n^m \left| \frac{\partial}{\partial \mu} (U\delta_{LS}) \right. \right\rangle, \end{aligned} \quad (11)$$

$$\begin{aligned} \frac{dD_n^m}{dt} = & 2d_{m,n}\zeta_{n-1}^m + 2d_{m,n+1}\zeta_{n+1}^m - 2U_n^m + D_{\tau n}^m - A_M n(n+1)D_n^m \\ & + \frac{n(n+1)}{Fr^2} h_n^m - \frac{1}{\tau_c} \left\langle Y_n^m \left| im \frac{U\delta_{LS}}{1-\mu^2} \right. \right\rangle - \frac{1}{\tau_c} \left\langle Y_n^m \left| \frac{\partial}{\partial \mu} (V\delta_{LS}) \right. \right\rangle, \end{aligned} \quad (12)$$

$$\frac{dh_n^m}{dt} = -D_n^m - \left\langle Y_n^m \left| im \frac{U(H-1)}{1-\mu^2} \right. \right\rangle - \left\langle Y_n^m \left| \frac{\partial}{\partial \mu} [V(H-1)] \right. \right\rangle, \quad (13)$$

$$U_n^m = -\frac{n-1}{n(n-1)} d_{m,n}\zeta_{n-1}^m + \frac{n+2}{(n+1)(n+2)} d_{m,n+1}\zeta_{n+1}^m - \frac{im}{n(n+1)} D_n^m, \quad (14)$$

$$\begin{aligned} V_n^m = & -\frac{im}{n(n+1)} \zeta_n^m + \frac{n-1}{n(n-1)} d_{m,n} D_{n-1}^m \\ & - \frac{n+2}{(n+1)(n+2)} d_{m,n+1} D_{n+1}^m, \end{aligned} \quad (15)$$

where $C_{\tau n}^m$ and $D_{\tau n}^m$ are the spectral coefficients for wind stress curl $-\nabla \cdot (\mathbf{k} \times \boldsymbol{\tau}/H)$ and wind stress divergence $\nabla \cdot (\boldsymbol{\tau}/H)$, respectively. The coefficients $d_{m,n}$ are defined by

$$d_{m,n} = \sqrt{\frac{n^2 - m^2}{4n^2 - 1}}. \quad (16)$$

The terms in angle brackets are associated with the continental drag and variable ocean depth. As their determination demands many steps of calculation, we apply an efficient spectral transform method (Orszag, 1970; Machenhauer and Rasmussen, 1972).

For practical purposes the expansion (10) will be truncated at a certain total wavenumber N (triangular truncation); with M latitudes, it is necessary to truncate at wavenumber $N = (2M - 1)/3$ to avoid aliasing due to bilinear products.

The equations are time integrated with an implicit scheme to enable large time-steps; that is, terms, which are not associated with wind stress, are integrated with the Euler backward time integration method. In addition, the terms associated with high drag by continents should be treated implicitly to ensure stability for a continental friction timescale τ_c much smaller than one time-step interval. The implicit time integration scheme of SOM is described in more detail in the Appendix A.

4. Determination of steady solutions

The model equations in spectral representation form a system of inhomogeneous linear ordinary differential equations of first order. They can, therefore, be written in the following form:

$$\frac{d\mathbf{X}}{dt} = \mathbf{A} \cdot \mathbf{X} + \mathbf{F}_\tau, \quad (17)$$

where $\mathbf{X} = (\zeta_1^0, D_1^0, h_1^0, \zeta_2^0, D_2^0, h_2^0, \dots, \zeta_1^1, D_1^1, h_1^1, \zeta_2^1, D_2^1, h_2^1, \dots)$ is a state vector composed of all spectral coefficients for vorticity, divergence, and height; \mathbf{A} is a matrix and \mathbf{F}_τ a vector composed of wind forcing terms. We can derive a steady state solution by inverting the matrix \mathbf{A} :

$$\mathbf{X} = -\mathbf{A}^{-1} \cdot \mathbf{F}_\tau. \quad (18)$$

Furthermore, for a uniform depth ocean the divergence D becomes zero; in this case the steady state flow is entirely determined by Eq. (11).

Sometimes it is convenient to consider the depth-weighted flow $\tilde{\mathbf{v}} \equiv H\mathbf{v}$ since the divergence of this vector field vanishes in the steady state even if the depth H of the ocean varies horizontally. Following Hasselmann (1982) the steady state vorticity equation can also be written as follows

$$\begin{aligned} \nabla \cdot \left[\mathbf{k} \times \left(\frac{2\mu}{H} \nabla \tilde{\psi} \right) - \frac{\delta_{LS}}{H\tau_c} \nabla \tilde{\psi} \right] \\ - A_M (\nabla^2 + 2) \left(\frac{1}{H} \nabla^2 \tilde{\psi} - \frac{1}{H^2} \nabla H \cdot \nabla \tilde{\psi} \right) = -\nabla \cdot \left(\mathbf{k} \times \frac{\boldsymbol{\tau}}{H} \right), \end{aligned} \quad (19)$$

where $\tilde{\psi}$ is the streamfunction of the depth-weighted flow. Compared to system (17), fewer equations result when the vorticity Eq. (19) is presented in spectral form:

$$\begin{aligned} \left\langle Y_n^m \left| \frac{im}{1-\mu^2} \left(\frac{2\mu}{H} \tilde{U} + \frac{\delta_{LS}}{H\tau_c} \tilde{V} \right) \right. \right\rangle \\ - \left\langle Y_n^m \left| \frac{\partial}{\partial \mu} \left(-\frac{2\mu}{H} \tilde{V} + \frac{\delta_{LS}}{H\tau_c} \tilde{U} \right) \right. \right\rangle + A_M [n(n+1)-2] \zeta_n^m = C_{\tau n}^m, \end{aligned} \quad (20)$$

where (\tilde{U}, \tilde{V}) is the depth-weighted velocity that will be determined by the spectral relations

$$\tilde{U}_n^m = (n-1)d_{m,n}\tilde{\psi}_{n-1}^m - (n+2)d_{m,n+1}\tilde{\psi}_{n+1}^m, \quad (21)$$

$$\tilde{V}_n^m = im\tilde{\psi}_n^m. \quad (22)$$

The vorticity coefficients ζ_n^m result from the equation

$$\zeta_n^m = \left\langle Y_n^m \left| \frac{im}{1-\mu^2} \frac{1}{H} \tilde{V} \right. \right\rangle - \left\langle Y_n^m \left| \frac{\partial}{\partial \mu} \left(\frac{1}{H} \tilde{U} \right) \right. \right\rangle. \quad (23)$$

Inversion of Eq. (20) gives the spectral coefficients for the streamfunction $\tilde{\psi}$ that suffices to determine the complete flow field. Finally, to specify the steady state solution, the matrix \mathbf{A} is inverted using the LAPACK package.

5. Numerical simulations by SOM: Idealized and realistic ocean basins

This section presents five sets of numerical simulations with T63 resolution:

- a. wind-driven flow in an idealized basin,
- b. wind-driven flow in realistic ocean basins with and without bathymetry,
- c. equatorial wave dispersion and reflection in an idealized basin,
- d. gravity wave propagation in the Pacific with real bathymetry,
- e. tracer advection in an idealized basin.

5.1. Idealized basins and wind forcing

In the first set of simulations we prescribe a simple basin geometry by setting the land–sea mask function

$$\delta_{LS}(\lambda, \mu) = 0.5 \left[\tanh \left(\frac{|\lambda| - \pi/2}{\delta\lambda} \right) + 1 \right]. \quad (24)$$

Note that the idealized basin extends in zonal direction from $\lambda_w = 90^\circ$ W to $\lambda_e = 90^\circ$ E. The width of the transition layer between land and ocean is proportional to $\delta\lambda$ for which we choose the value 0.02. We set δ_{LS} to zero when the value (as calculated by Eq. (24)) is below 0.01 in order to eliminate spurious friction in the interior ocean.

The continental friction timescale τ_c is 720 times smaller than the integration time-step of $\Delta t^* = 1$ day. For the dimensional zonal

wind stress τ_λ^* we introduce a simple zonally symmetric field given by

$$\tau_\lambda^* = -0.1 \text{ Nm}^{-2} \cos(3\varphi), \quad (25)$$

while the meridional wind stress is set to zero. The depth of the ocean is constant with $H_0 = 5000$ m. We assume Earth-like conditions; that is, we set gravity acceleration $g = 9.81 \text{ m/s}^2$, Earth rotation rate $\Omega = 7.292 \times 10^{-5} \text{ s}^{-1}$, and Earth radius $a = 6371$ km. Consequently, the Froude number becomes $Fr \approx 2.1$. We choose for the dimensional momentum exchange coefficient $A_M^* = 5 \times 10^5 \text{ m}^2/\text{s}$.

The steady state circulation as simulated by SOM should resemble Munk's (1950) analytical solution. This rests upon the assumption that horizontal eddy momentum exchange becomes relevant only in the boundary layers, namely, at the western and eastern coasts, where the eddy momentum exchange is predominantly directed in the zonal direction. In this case the steady state vorticity equation becomes

$$\left(2 \frac{\partial}{\partial \lambda} - \frac{A_M}{(1 - \mu^2)^2} \frac{\partial^2}{\partial \lambda^4} \right) \psi = -\nabla \cdot (\mathbf{k} \times \boldsymbol{\tau}). \quad (26)$$

The analytical solution of this equation fulfilling approximately no-slip boundary conditions reads

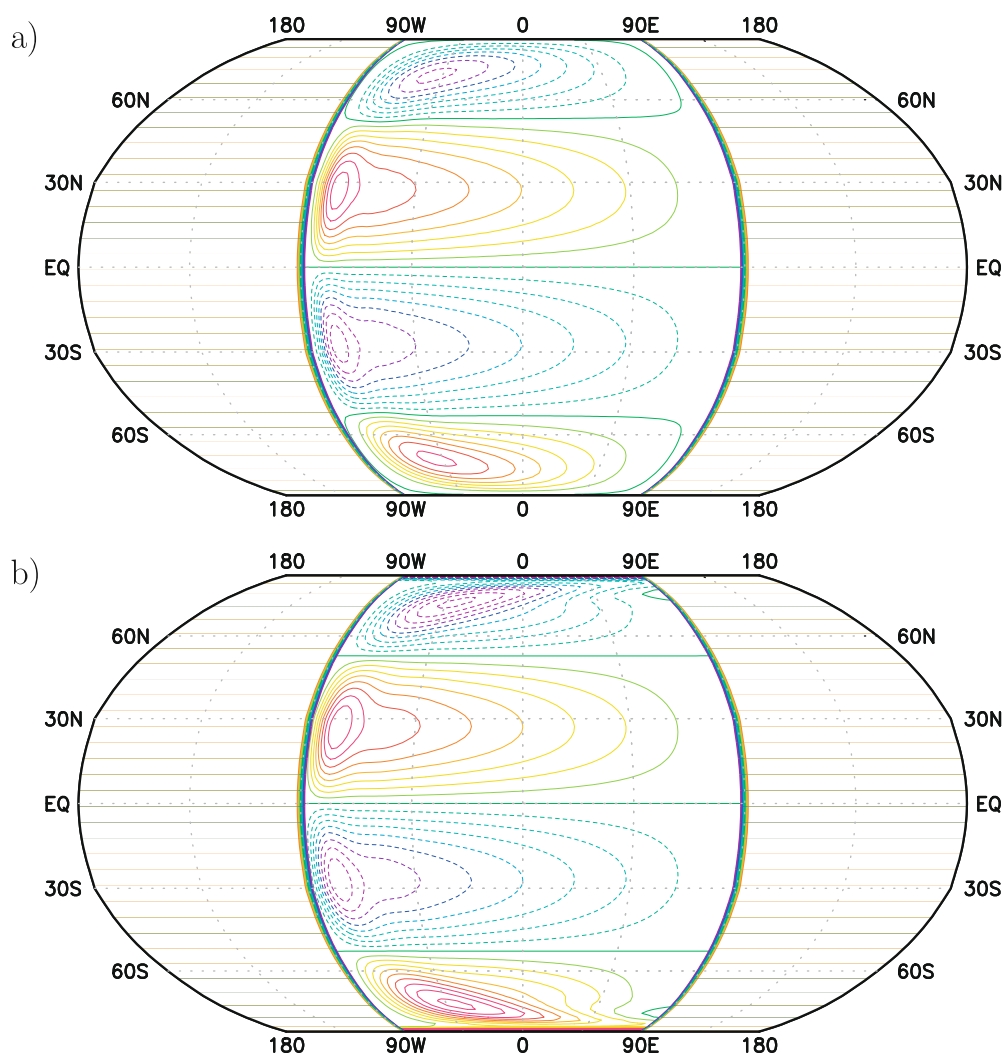


Fig. 1. Streamfunction of the vertically integrated flow in the idealized basin for (a) SOM at $t = 90$ days and (b) Munk's analytical solution. The shaded regions near 90° W and 90° E are associated with the transition zones between land and ocean. The contour interval is 1 Sv and negative isolines are dashed.

$$\psi = -\frac{1}{2} \nabla \cdot (\mathbf{k} \times \boldsymbol{\tau}) \left\{ \underbrace{\lambda' - \Delta_B + \Delta_M}_{\Phi_i} - \underbrace{\Delta_M e^{(\lambda' - \Delta_B)/\Delta_M}}_{\Phi_e} + e^{(-\lambda'/2\Delta_M)} \left[(\Delta_B - \Delta_M) \cos\left(\frac{\sqrt{3}}{2} \frac{\lambda'}{\Delta_M}\right) + \frac{\Delta_B - 3\Delta_M}{\sqrt{3}} \sin\left(\frac{\sqrt{3}}{2} \frac{\lambda'}{\Delta_M}\right) \right] \right\}, \quad (27)$$

where $\lambda' = \lambda - \lambda_w$. The widths of the basin and the Munk layer are given by $\Delta_B = \lambda_e - \lambda_w$ and $\Delta_M = [A_M/(1 - \mu^2)/2]^{1/3}$, respectively. Munk presumed that $\Delta_M \ll \Delta_B$. Thus, the streamfunction of the eastern and western boundary layer partial solutions Φ_e and Φ_w can be neglected at the western and eastern coasts, respectively. Nevertheless, Munk's solution becomes invalid near the poles where the assumption $\Delta_M \ll \Delta_B$ does not hold. Note that $1/2\Phi_i$ times the wind stress curl gives the streamfunction of the interior flow, which follows an exact Sverdrup balance.

Fig. 1a displays the mass streamfunction simulated by SOM when the model attains steady state after 90 days. Indeed, solving Eq. (20) gives a circulation pattern identical to that shown in Fig. 1a: On each hemisphere a cyclonic and an anticyclonic gyre evolves which corresponds to the fields of cyclonic and anticyclonic wind stress curl, respectively. Fig. 1b shows the mass stream function of Munk's solution. The SOM results agree very well with those given by Munk's solution except near the poles, where Munk's solution becomes incorrect. A comparison of the meridional velocity at 30°N of SOM and Munk's solutions is presented in Fig. 2 for $A_M^* = 2, 5, \text{ and } 10 \times 10^5 \text{ m}^2/\text{s}$. The western boundary layer (the Munk layer) comprises a northward flow near the coast line juxtaposed to the east by a recirculating southward flow. In the interior ocean the meridional velocity is nearly constant and takes the value predicted by the Sverdrup balance. Near the eastern shore southward flow is decelerated due to eastward momentum transfer in a thin boundary layer. SOM also simulates these features fairly well; only near the western coast some differences become apparent. Firstly, the flow west of the velocity maximum is too weak compared to Munk's solution because the strong viscosity at coastlines decelerates the flow in a transition zone of finite width. Therefore, additional drag by continents decelerates the flow near the coast line. Secondly, the maximum of the northward flow in SOM is too large and, compared to Munk's solution, lies too far to the east. Since the vorticity is smaller near the coast line in SOM less momentum is transported westward than in Munk's solution. This might explain the difference in the flow maximum. Thirdly, for $A_M^* = 2 \times 10^5 \text{ m}^2/\text{s}$ a Gibbs phenomenon occurs that becomes visible as several alternating maxima and minima in the velocity profile. For this small momentum exchange coefficient the Munk layer width Δ_M is too thin to be properly represented by T63 spectral truncation. An alternative is to use a higher order diffusion operator (hyperdiffusion) for the parameterization of horizontal eddy momentum transfer.

5.2. Wind-driven world ocean with uniform and varying depth

A further step is to test the capability of simulating the flow in arbitrarily shaped basins by SOM. We take the real land–sea mask of the Earth and drive the oceanic flow with observed climatological wind stresses (Hellerman and Rosenstein, 1983). In order to obtain thin transition zones between land and ocean we smoothed the primarily discontinuous land–sea mask. The real ocean depth has been interpolated to T63 and slightly smoothed. The minimum depth is prescribed to 100 m to obtain finite wind stress values. Fig. 3 shows the wind stress vectors, the depth field and the land–sea mask. We performed two experiments, one with constant

depth 5000 m (CONDEPTH) and the other with varying depth as given in Fig. 3 (VARDEPTH). Similar experiments were performed by Bryan and Cox (1972).

The full spin-up of the wind-driven circulations of both experiments is, as in the idealized basin case, completed after 90 days. Fig. 4 shows the streamfunction fields for experiment CONDEPTH and VARDEPTH after day 90. The circulation patterns closely resemble the steady state solutions of Eq. (20) (not shown). Anticyclonic and cyclonic gyres can be seen in the different ocean basins which are characterized by Sverdrup balance in the interior and a Munk layer at the western shores in CONDEPTH (Fig. 4a). The mass transport by these gyres has the same magnitude as in Bryan and Cox (1972). However, the dominating mass transport is by the Antarctic Circumpolar Current (ACC) in CONDEPTH with of almost 200 Sv. Bryan and Cox (1972) even simulated a the mass transport of the ACC which exceed 600Sv due to their smaller horizontal momentum exchange coefficient. For VARDEPTH the streamlines are distorted by bottom orography. Considering Eq. (19) gives the generalized Sverdrup relation after neglecting viscosity terms (see Hasselmann, 1982). In this relation the gradient of f/H (with Coriolis parameter $f = 2\mu$) comes into play instead of the planetary vorticity gradient that appears in the classical Sverdrup relation. Therefore, the streamlines tend to align f/H contours (Fig. 5). The main consequence of using a varying ocean depth is the breakdown of the ACC which is consistent with other studies (Bryan and Cox, 1972; Olbers and Eden, 2003).

For comparison, Fig. 4c displays the mass stream function obtained from the mean state of GECCO (German partner of “Estimating the Circulation and Climate of the Ocean” (ECCO) consortium effort) reanalysis data. GECCO reanalysis is based on the first global ECCO adjoint estimate with 1° horizontal resolution. It spans the period 1952–2001 and combines most of the global observations available during entire estimation period with the ECCO adjoint model so as to simulate best the observed ocean state (Stammer et al., 2004 and Köhl et al., 2006, 2007). The curl of the depth-integrated GECCO flow has been interpolated on a Gaussian grid corresponding to T170 spectral truncation. Afterwards, the streamfunction is determined in spectral space by inversion of the Laplacian. A comparison with Fig. 4a and b reveals that all observed wind-driven currents are reproduced with SOM. However, the strength of the currents turns out to be weaker in SOM than in the GECCO reanalysis. Obviously, mass transports of CONDEPTH experiments are in better agreement with GECCO data. Especially, the ACC in CONDEPTH has a similar magnitude while it is much weaker in VARDEPTH. The differences of VARDEPTH to GECCO may partially be explained by the absence of baroclinic terms in SOM. These can shield the effects of the bottom topography when the flow speed becomes zero at the bottom.

Fig. 6 shows the time evolution of the mass transport by the ACC, Kuroshio (western boundary current in the North Pacific), and the Gulf Stream (western boundary current in the North Atlantic). The mass transports by the Kuroshio and the Gulf Stream equilibrate already after 20 days in both experiments. The simulated adjustment time and the magnitudes of these currents agree with the findings of Bryan and Cox (1972). The mass transport of the ACC equilibrates after 90 days in CONDEPTH and after 20 days

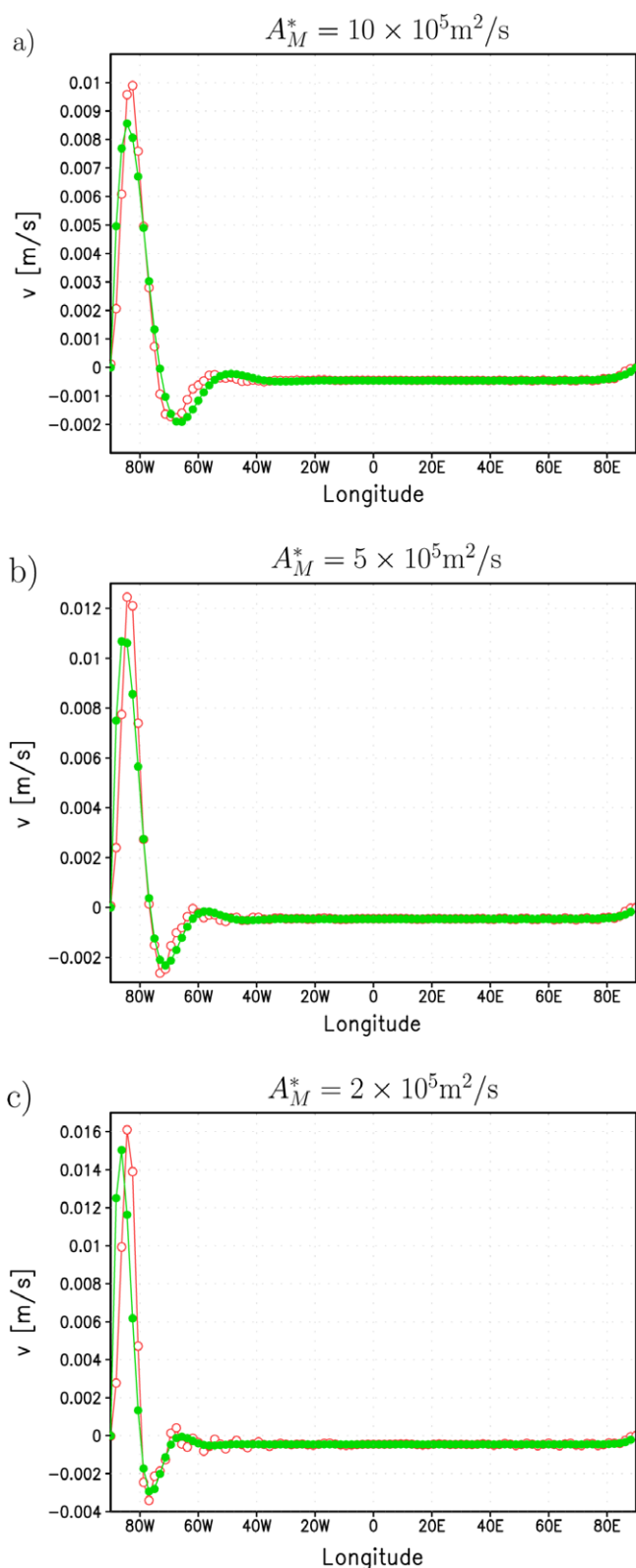


Fig. 2. Meridional velocity of the depth-averaged flow in the idealized basin at 30°N for (a) $A_M^* = 10 \times 10^5 \text{ m}^2/\text{s}$, (b) $A_M^* = 5 \times 10^5 \text{ m}^2/\text{s}$, and (c) $A_M^* = 2 \times 10^5 \text{ m}^2/\text{s}$. Open circles show the result of SOM and filled circles that of Munk's solution.

in VARDEPTH. It is noteworthy that the ACC transport is much weaker in VARDEPTH. In summary, SOM can simulate the wind-driven flow of arbitrarily shaped basins realistically if the model resolution is high enough to resolve these basins, and the results

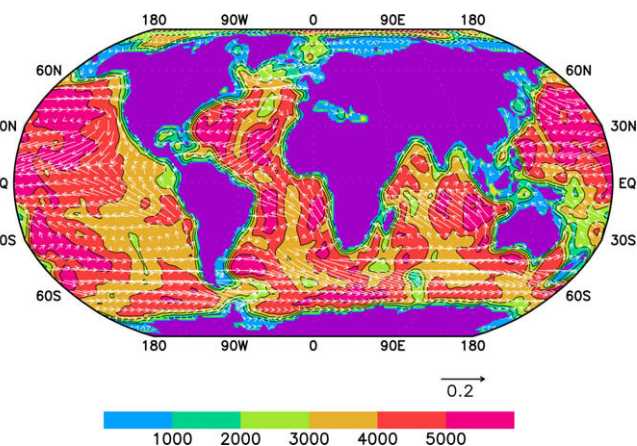


Fig. 3. Ocean depth (coloured shadings in m), wind stress (vectors in N/m^2), and land-sea mask (overlaid shadings).

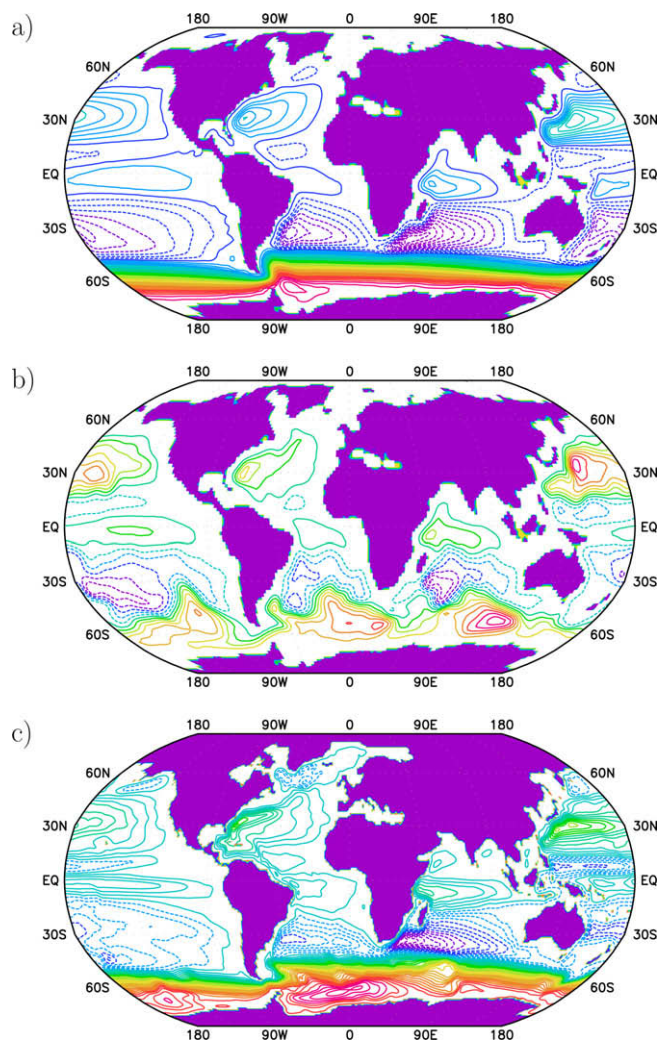


Fig. 4. Streamfunction of the vertically integrated flow of the wind-driven world ocean after $t = 90$ days for (a) experiment CONDEPTH, (b) experiment VARDEPTH and (c) GECCO reanalysis (time average 1952–2001). The contour interval is 5 Sv and negative isolines are dashed.

are in general agreement with the outcome of other studies based on grid-point models (Sag, 1969; Leichtmann et al., 1971; Bryan and Cox, 1972; Olbers and Eden, 2003).

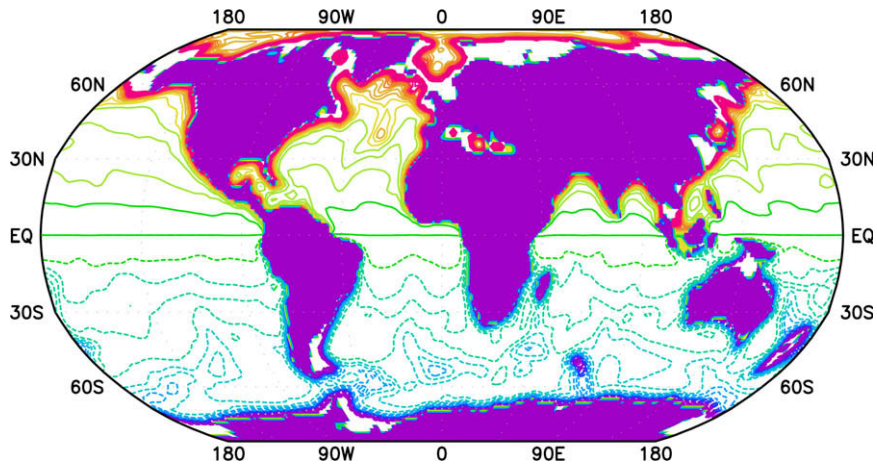


Fig. 5. Contours of f/H (contour interval 0.25). Negative values are associated with dashed isolines.

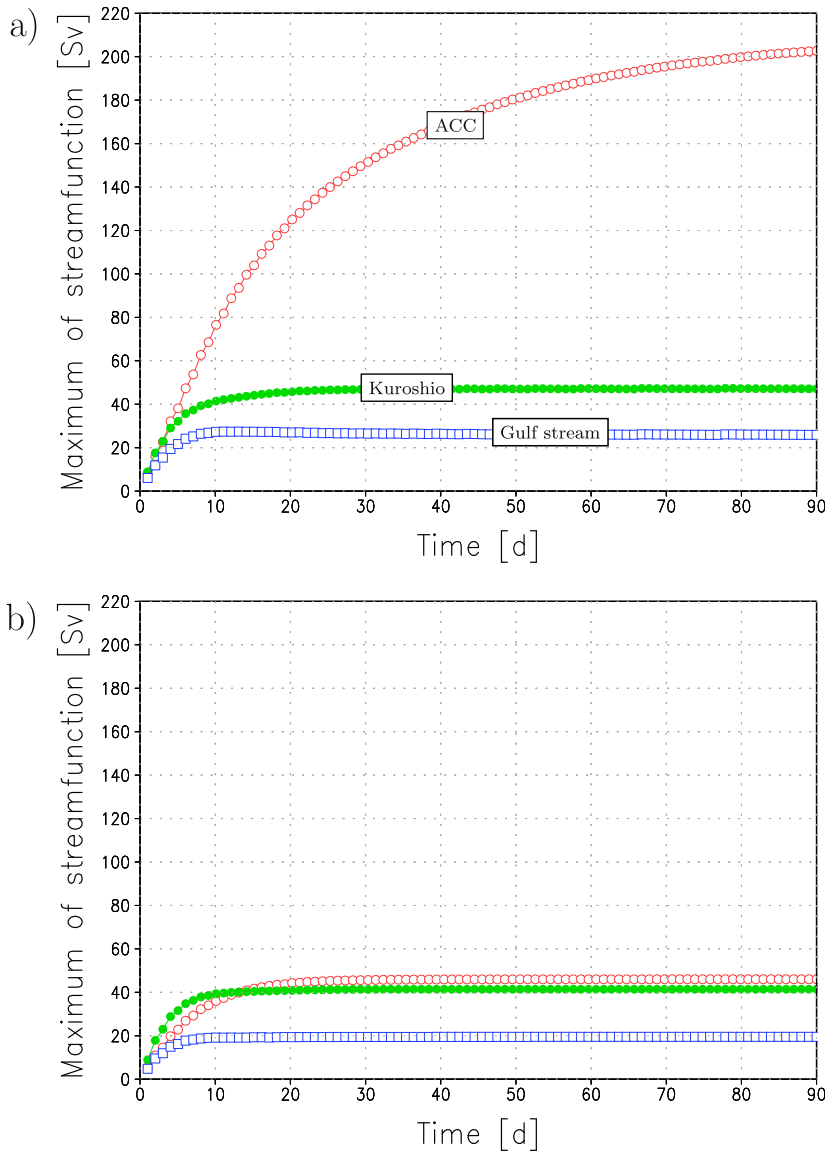


Fig. 6. Mass transport (in Sv) of the Antarctic Circumpolar Current (open circles), of the Kuroshio (North Pacific, filled circles) and of the Gulf Stream (North Atlantic, open squares) for (a) experiment CONDEPTH and (b) experiment VARDEPTH.

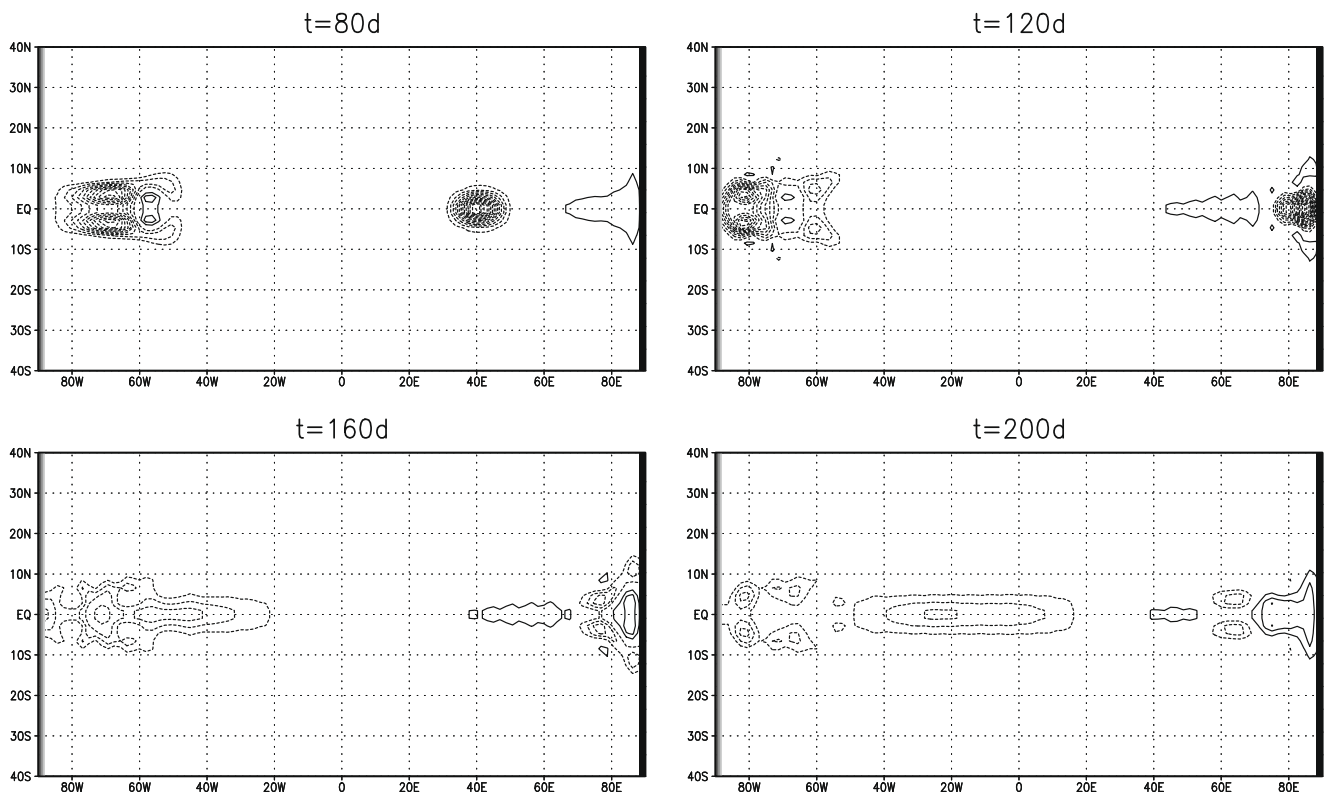


Fig. 7. Dispersion and reflection of equatorial waves as simulated by SOM. Height anomaly at $t = 80$, $t = 120$, $t = 160$ and $t = 200$ days in a simulation initialized by a height anomaly centered at the equator. The contour interval is 0.05 m and negative height values are associated with dashed isolines. The shaded regions near 90°W and 90°E are associated with the transition zones between land and ocean.

5.3. Dispersion and reflection of equatorially trapped waves

In this section we want to test if SOM is capable of reproducing characteristics of equatorial waves and their reflection at meridional boundaries; which are important when simulating the climate phenomenon El Niño Southern Oscillation. To serve this purpose we conduct a wave dispersion experiment as suggested by Philander et al. (1984). We initialize the model with a height anomaly of the form:

$$h = -h_0 \exp \left\{ -a^2 \left[(\lambda - \lambda_0)^2 + (\varphi - \varphi_0)^2 \right] / \Delta r^2 \right\}, \quad (28)$$

where h_0 is the amplitude. The parameters specifying the anomaly are $\lambda_0 = -\pi/4$, $\varphi_0 = 0$ and $\Delta r = 500$ km. The longitude of the anomaly (this corresponds to 45°W). That is, the initial height anomaly has the shape of a Gaussian bell. Philander et al. (1984) considered a reduced gravity model with $g = 0.02$ m/s² and $H_0 = 98$ m. With this setup the phase speed of gravity waves attains 1.4 m/s and assuming the other parameters the same as before we obtain the Froude number $\text{Fr} = 331.84$. To minimize damping, the horizontal momentum exchange coefficient A_M is set to zero. Instead, a 4th order hyperdiffusion term ($\propto \nabla^8$) is added to the vorticity and divergence equations. The hyperdiffusion coefficient is chosen so that the damping timescale yields 5 days for the spectral coefficients at the truncation wavenumber (total wavenumber 63). The basin geometry is the same as given by Eq. (24) but the time-step is much shorter with $\Delta t^* = 1$ h. The impact of larger time-steps is analyzed below. In this basin, we expect reflection of equatorial waves at both meridional walls, which are well captured by SOM as shown by Figs. 7 and 8.

Fig. 7 displays the height anomaly after 80, 120, 160, and 200 days of the simulation. After 80 days the initial bell-shaped anomaly has split into an eastward traveling Kelvin wave with meridio-

nal monopole structure and a westward traveling Rossby wave with a meridional dipole structure. At day 120, both anomalies reach the boundaries. At day 160, the Rossby wave is reflected at the western boundary in form of Kelvin waves while the Kelvin wave is reflected at the eastern boundary in form of a Rossby wave. However, some anomalies remain trapped as coastal Kelvin waves at the eastern boundary; not all Rossby wave energy has reached the western boundary due to Rossby wave dispersion. By $t = 200$ days, the reflected waves have traveled far away from the coasts and their identification as Rossby and Kelvin waves is clearly evident.

The reflection of the Kelvin wave looks similar to that obtained by Soares et al. (1999) using a high resolution grid-point model. However, the energy loss due to the reflection is higher in SOM, because the continental drag at the boundaries exerts a strong damping on the incident wave. Fig. 8a shows a longitude-time (Hovmöller) diagram of the zonal velocity at the equator. Obviously, the eastward propagating Kelvin wave does not disperse and the phase speed is exactly 1.4 m/s as predicted by theory (Matsuno, 1966). High frequency inertia-gravity waves are evident in the westward migrating wave packet but they are rapidly damped by the implicit time-stepping. The Rossby wave packet exhibits dispersion while the Kelvin wave remains unchanged. The phase speed of the former is roughly one third of the Kelvin wave phase speed. This is consistent with the phase speed of the first equatorially trapped Rossby wave mode after applying the long wave approximation (Gill and Clarke, 1974).

The damping of the waves increases with a larger time-step as shown in Fig. 8b for $\Delta t^* = 24$ h. An alternative to the implicit time integration scheme is the semi-implicit leap-frog scheme (Hoskins and Simmons, 1975). With this scheme waves are not damped but the frequencies become erroneous for too large time-steps. Fig. 8c

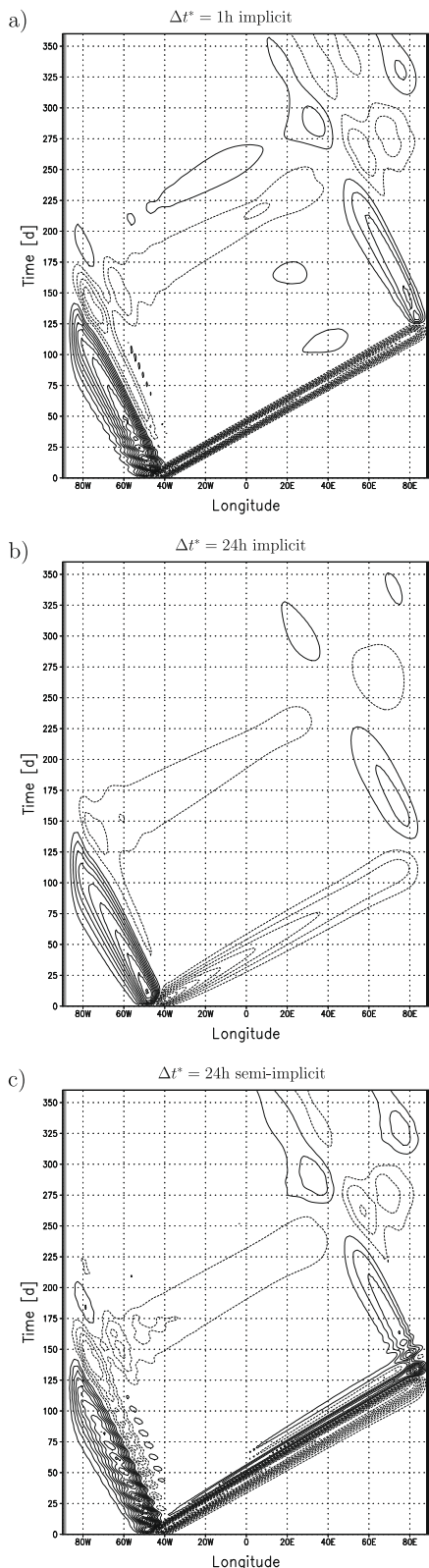


Fig. 8. Longitude-time (Hovmöller) diagram along the equator for the zonal velocity in the equatorial wave simulation for (a) $\Delta t^* = 1$ h, (b) $\Delta t^* = 24$ h, (c) $\Delta t^* = 24$ h using the semi-implicit time integration scheme. The contour interval is 0.0005 m/s and negative zonal velocities are associated with dashed isolines.

shows the Hovmöller diagram for an integration with the semi-implicit scheme. Now, the eastward propagating Kelvin wave shows slight dispersion. We conclude that the semi-implicit

scheme appears to be the better choice for simulations where wave dynamics is important although group velocities are not exactly simulated.

5.4. Propagation of surface gravity waves in the Pacific ocean basin

In this experiment we demonstrate that SOM simulates the propagation of surface gravity waves suitably. For this purpose SOM is initialized with a height anomaly given by Eq. (28) where $\Delta r = 166.7$ km. The position of this anomaly is at $\lambda = 178^\circ$ E and $\varphi = 52^\circ$ N and the real bathymetry of the Pacific Ocean is incorporated in the model. We choose a high spectral truncation at total wavenumber 170 (T170) to resolve the excited wave packet reasonably. Since the inversion of the matrix is too costly at this high resolution we calculate tendencies by an explicit method. This experiment is a rough simulation of the so-called Rat Island tsunami at November 17, 2003 for which a successful real-time forecast was provided with a numerical tsunami model (Titov et al., 2005). We note that our model is still too coarse for a realistic simulation of tsunami waves and their run-up at the coasts. However, the simulated travel times are comparable to reality.

Fig. 9 displays the height anomaly after 0, 2, 4 and 6 h of the simulation. The wave packet is initially excited at the Aleutian ridge and spreads in all directions where an enhancement of wave height can be detected over the ridge and in the shallow water at 2 h. After 4 h the wave crosses the 25° latitude circle and reaches the coast of Japan. This is in agreement with the forecast by Titov et al. (2005) (see their Fig. 7). An increase of wave height and a slower propagation in shallow ocean regions also becomes evident. The wave has passed the Hawaiian islands two hours later. There, observations by the Hilo tide gauge indicate an arrival of the wave packet at about 5 h and 20 min with a maximum wave amplitude of 0.2 m. A comparison with the tide gauge record (Fig. 8 in Titov et al., 2005) shows that the maximum wave length is much longer in SOM than in reality. But beside this shortcoming which is due to the coarse resolution, SOM simulates the travel times of real tsunami waves reasonably well.

5.5. Tracer advection in an idealized basin

Advection of temperature and salinity is very important for a baroclinic ocean circulation. In the present barotropic model, however, temperature and salinity have no impact for the depth-averaged flow. Nevertheless, we are able to demonstrate the capability of SOM to simulate tracer advection reasonably. For this purpose the following nondimensional tracer transport equation will be solved numerically:

$$\frac{\partial T}{\partial t} + \nabla \cdot (\mathbf{v}T) - TD = A_T \nabla^2 T + Q_T \quad (29)$$

where T is an inactive tracer, A_T the diffusive exchange coefficient of this tracer and Q_T the sources and sinks of this tracer. This equation can be easily written in spectral representation, in which nonlinear advections terms are evaluated by the spectral transform method.

For tracer simulation we prescribe the flow by the wind-driven circulation in the idealized basin for $A_M^* = 5 \times 10^5$ m²/s (see Section 5.1) and the dimensional diffusive tracer exchange coefficient is selected to be $A_T^* = 500$ m²/s. The velocity components have been multiplied by the factor 10 to obtain realistic flow speeds for horizontal advection near the ocean surface. In the first experiment the source term Q_T for the tracer is a linear relaxation towards an equilibrium state T_e with the timescale τ_R , that is, $Q_T = (T - T_e)/\tau_R$. With this source term the tracer field may reach a steady state in which Q_T balances advection and diffusion. We prescribe the equilibrium tracer field T_e by

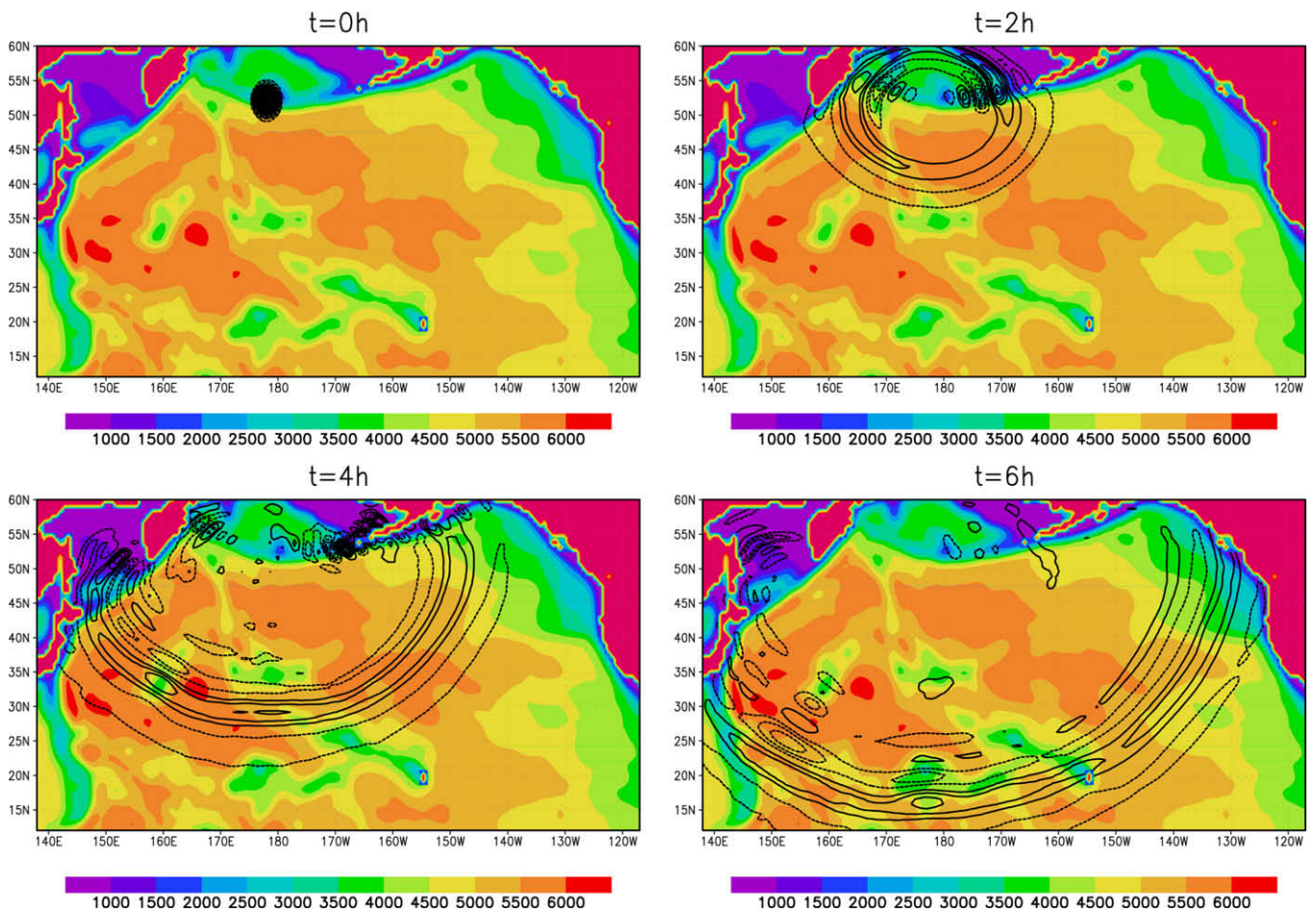


Fig. 9. Gravity wave propagation as simulated by SOM. Ocean depth (coloured shadings) and height anomaly (black isolines) at $t = 0$ h (contour interval 0.05 m), $t = 2$ h (contour interval 0.05 m), $t = 4$ h (contour interval 0.02 m) and $t = 6$ h (contour interval 0.02 m) in a simulation initialized with a height anomaly centered at 52° N and 178° E. Negative height values are associated with dashed isolines.

$$T_e = 30 \cos(\varphi) \quad (30)$$

and the timescale by $\tau_R^* = 720$ days. With this choice the time, velocity and tracer magnitudes are reasonable for the case that the mixed layer temperature is the tracer. Then, Q_T can be interpreted as a relaxation to equilibrium by radiation. In a second experiment we set $Q_T = 0$ to zero to simulate tracer transport without sources and sinks.

The tracer field is initialized with $T = T_e$ after the ocean spin-up (100 days) and the model is integrated for 3650 days (10 years). In the first experiment the tracer field attains a steady state roughly after 8 years. Fig. 10a displays the tracer field at the end of the simulation. A sharp east–west oriented front appears at 52° N near the western boundary. The formation of this front is not surprising since the flow field is strongly confluent in this region due to northward and southward boundary currents of the anticyclonic and cyclonic gyres (see Fig. 1a). The magnitude of the midlatitude meridional tracer gradient is slightly smaller in the eastern part of the basin, where the flow is diffluent due to Sverdrup balance, than over the adjacent land. Over land the tracer field nearly coincides with the equilibrium field T_e , because only diffusion acts there, which has a weak effect. In the second experiment (Fig. 10b) no sources and sinks occur. This has the impact that the tracer front becomes sharper and longer while the meridional gradient in the eastern part of the basin is weaker than in the experiment with nonzero Q_T . Furthermore, no steady state tracer field establishes within the 10 year period, since changes due to diffusion do not decline before the tracer field becomes uniform. In this simulation

the area average over the ocean basin should be conserved because the flow is nearly nondivergent. However, due to diffusion tracer may be transported through the coast lines which occurs mainly near the poles where latitude circles have a small circumference. For better conservation of area integrated quantities, a diffusion scheme needs to be implemented with the exchange coefficient A_T approaches zero at the coast lines. This will be tested in an improved model version.

A further alternative for calculation of tracer advection is the use of a semi-Lagrangian transport scheme. Such schemes are also implemented in atmospheric spectral GCMs like the ECHAM-5 model for a better simulation of the water vapor transport (e.g. Roeckner et al., 2003). As in the ECHAM-5 model we apply the flux-form semi-Lagrangian (FFSL) transport algorithm of Lin and Rood (1996). It preserves volume integrated quantities, the positive definiteness of mass densities as well as constant fields. We repeated the second experiment ($Q_T = 0$) with SOM in which advection is calculated with the FFSL scheme and diffusion is neglected. The latter is justified by the fact that the FFSL scheme already introduces some amount of diffusion to properly smooth the fields. Fig. 10c displays the tracer field after 10 years for this experiment and it becomes evident from this figure that the gradient at the tracer front becomes larger compared to the simulation in which advection is calculated with the spectral method (Fig. 10b). Furthermore, the cold and warm tongues do not reach as far to the east as found in Fig. 10b. These results are consequence of less diffusive mixing by the FFSL scheme. A clear advantage of the FFSL scheme is that no tracer fluxes occur across the

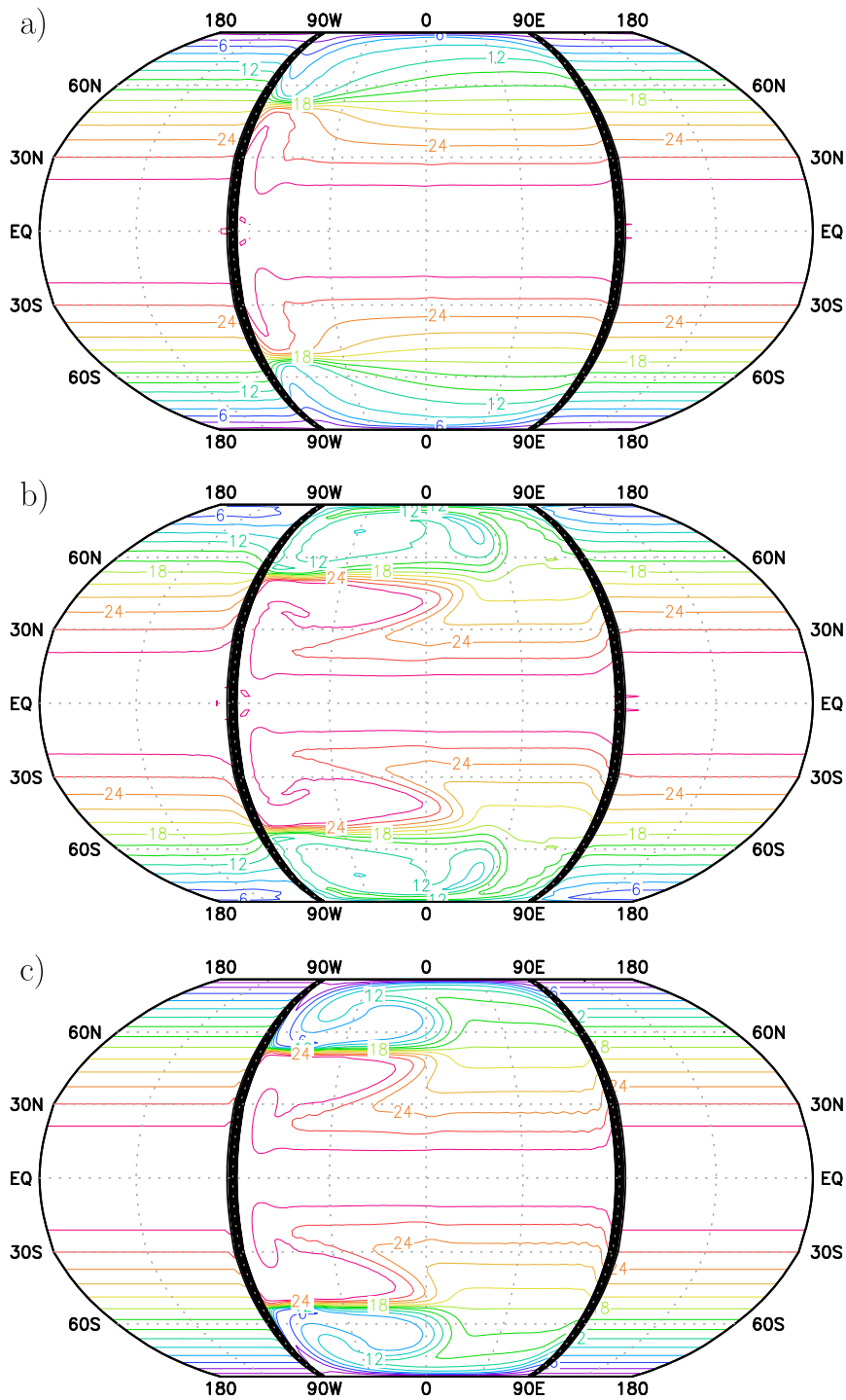


Fig. 10. Tracer T after 3650 days in the idealized ocean basin (contour interval 3) for (a) experiment 1 ($Q_T = (T_e - T)/\tau_R$) and (b) experiment 2 ($Q_T = 0$), (c) as (b) but for an integration in which advection is calculated with the semi-Lagrange transport scheme. The shaded regions near 90°W and 90°E are associated with the transition zones between land and ocean.

coast lines. Therefore, the volume integrated tracer mass of the ocean basin will be conserved which is advantageous for the simulation of salinity fields.

Inclusion of momentum advection should have no effect for the simulated depth-averaged flow due to the very low Reynolds number (based on the high horizontal momentum exchange coefficient $A_M^* = 5 \times 10^5 \text{ m}^2/\text{s}$). However, we foresee no problem due to the inclusion of momentum advection in the model since tracer advection is working quite well with a much smaller exchange coefficient ($A_T^* = 500 \text{ m}^2/\text{s}$). Indeed, the repetition of the idealized

wind-driven ocean experiment with momentum advection $\mathbf{v} \cdot \nabla \mathbf{v}$ included as an explicit term in the time scheme reveals virtually no effect on the circulation pattern and its evolution.

6. Conclusion and outlook

The spectral approach, though common for atmospheric general circulation models (A-GCM) and numerical weather prediction since the seventies, has not been seriously considered as a

viable tool to simulate the global ocean circulation. Here we present a first step towards a unified spectral atmosphere–ocean general circulation model (AO-GCM). For climate modelling a spectral model has several advantages. A seamless coupling to a spectral atmospheric global circulation is possible due to the identical grid structure and the longitude–latitude grid singularities at the poles do not cause problems. Furthermore, filtering of wave dynamics as in a Large Scale Geostrophic ocean model can be done with less effort since the inversion of operators in spectral space is more efficient and often more convenient. We apply the spectral method to a global ocean general circulation model (O-GCMs), starting with the depth-averaged version of the Large Scale Geostrophic (LSG) system (as suggested by Hasselmann (1982) and presented by Maier-Reimer et al., 1993). The following results are obtained:

1. The barotropic depth-averaged model equations are cast in spectral form using vorticity and divergence (instead of horizontal momentum) equations with nearly infinite drag exerted by the continents. The coding (including time integration) follows that of spectral A-GCMs using triangular truncation like PUMA or Planet Simulator (Fraedrich et al., 2005), which are freely available, or ECHAM (Roeckner et al., 2003).
2. Model performance is tested via four simulations, two of wind-driven ocean circulation and two of wave dynamics: (i) For idealized ocean basins, SOM simulates a wind-driven barotropic ocean circulation closely similar to Munk's analytical solution. (ii) With a real land–sea mask: SOM is capable of reproducing the spin-up, location and magnitudes of depth-averaged barotropic ocean currents, consistent with previous studies. (iii) For equatorial wave-dynamics in a reduced gravity setup, waves are excited by a height perturbation at the equator: SOM simulates fairly well the wave dispersion and reflection at both idealized meridional boundaries. (iv) For surface gravity wave-dynamics with real bathymetry: SOM successfully reproduces the travel times of real tsunami waves. (v) The advection of tracers can be reasonably well simulated by the spectral prescribing a moderate diffusion coefficient or by a semi-Lagrangian transport scheme without additional diffusion.

This group of experiments is suggested to serve as a test-set for dynamical cores of (barotropic) O-GCMs like the Held and Suarez (1994) test for the dynamical cores of A-GCMs.

In its present state SOM is a barotropic model for a uniform density ocean but it can also be used for a reduced gravity setup to roughly simulate the wind-driven flow near the ocean surface. In this sense it provides a simple model that can already be coupled to an atmosphere and employed for the study of atmosphere–ocean interactions in idealized contexts. The multi-layer version simulating baroclinic flows with and without large scale geostrophic filtering (introduced by Hasselmann, 1982) will be reported in a subsequent paper; this includes coupling with the Planet Simulator to provide a unified intermediate complexity spectral AO-GCM suitable for simulating and understanding long-term climate variability on timescales beyond millennia. Here it should be noted that we do not intend SOM to become a state-of-the-art complex ocean circulation model for simulating the large-small scale interactions in the real ocean circulation since the spectral and implicit time-stepping method becomes inefficient at very high spatial resolutions.

In this study we exclude horizontal momentum advection in the model equations but this can be included without much effort. With advection, SOM is also being applied as a stand alone model for analysis of turbulence decay in rotating tank experiments,

where momentum advection is due to nonlinear vortex interactions relevant for turbulent flow simulations.

Acknowledgements

The helpful comments by two anonymous reviewers are greatly appreciated. The code of the semi-Lagrangian transport scheme was provided by Dr. Hui Wan, whose assistance is gratefully acknowledged. Furthermore, the authors thank Detlef Stammer, Alfonso Sutera, Ernst Maier-Reimer, Zhengyu Liu, Stephen Griffies, Peter Herrmann, Frank Lunkeit, and Edilbert Kirk for helpful discussions. One of the authors (WW) is supported by the Deutsche Forschungsgemeinschaft (DFG) within the SPP 1257.

Appendix A. Time integration method

For time integration an implicit method is used which will be described in the following. All terms except for the wind stress are integrated with the Euler backward scheme. This scheme has also been adopted in the LSG model (Maier-Reimer et al., 1993) and has the advantage that it is unconditionally stable. Therefore, the time-step is not limited by the short periods of inertia-gravity waves or by high viscosity. Instead, high frequency oscillations are damped with this scheme. For simulations, where damping is not desirable, we developed an alternative scheme, in which terms associated with wave dynamics are integrated by a semi-implicit leap-frog scheme suggested by Hoskins and Simmons (1975). Implicit terms can be evaluated by matrix inversion, because the model equations are linear. We use three time levels to easily include nonlinear advection terms with an explicit leap-frog scheme. Computational modes are damped with a Robert/Asselin filter (Haltiner and Williams, 1980). Introducing this time discretization to the spectral model yields Eqs. (11)–(13) in vector form

$$\mathbf{X}_\zeta^{n+1} = \mathbf{X}_\zeta^{n-1} + 2\Delta t(\mathcal{L}^{n+1} + \mathcal{C}_\tau), \quad (\text{A.1})$$

$$\mathbf{X}_D^{n+1} = \mathbf{X}_D^{n-1} + 2\Delta t(\mathcal{D}^{n+1} + Fr^{-2}\mathbf{L} \cdot \mathbf{X}_h^{n+1} + \mathcal{D}_\tau), \quad (\text{A.2})$$

$$\mathbf{X}_h^{n+1} = \mathbf{X}_h^{n-1} + 2\Delta t(\mathcal{H}^{n+1} - \mathbf{X}_D^{n+1}), \quad (\text{A.3})$$

here, $\mathbf{X}_\zeta = (\zeta_1^0, \zeta_2^0, \dots)$, $\mathbf{X}_D = (D_1^0, D_2^0, \dots)$, and $\mathbf{X}_h = (h_1^0, h_2^0, \dots)$ denote the vectors composed of the respective spectral coefficients, Δt is the time-step, and the superindex gives the number of the time-step. The vectors \mathcal{L} , \mathcal{D} , \mathcal{H} are the respective tendencies due to the Coriolis force, bottom relief, viscosity and drag, while the vector terms \mathcal{C}_τ and \mathcal{D}_τ are associated with wind stress. \mathbf{L} is a diagonal matrix, in which the eigenvalues of the Laplace operator, multiplied with -1 , form the diagonal elements, that is, $L_{mm} = n(n+1)$. Since the model is linear we can write the terms \mathcal{L} , \mathcal{D} , and \mathcal{H} in matrix form. Note that these terms depend only on vorticity and divergence. Then, we can write, for example

$$\mathcal{L} = \mathbf{Z}_\zeta \cdot \mathbf{X}_\zeta + \mathbf{Z}_D \cdot \mathbf{X}_D, \quad (\text{A.4})$$

where \mathbf{Z}_ζ and \mathbf{Z}_D are matrices. Consequently, by inserting (A.3) into (A.2) and by moving the new values $(\cdot)^{n+1}$ to the left hand sides of the vorticity and the divergence equations, we obtain

$$\begin{pmatrix} \mathbf{E} - 2\Delta t\mathbf{Z}_\zeta & -2\Delta t\mathbf{Z}_D \\ -2\Delta t(\mathbf{D}_\zeta + \frac{2\Delta t}{Fr^2}\mathbf{L} \cdot \mathbf{H}_\zeta) & \mathbf{C} - 2\Delta t(\mathbf{D}_D + \frac{2\Delta t}{Fr^2}\mathbf{L} \cdot \mathbf{H}_D) \end{pmatrix} \cdot \begin{pmatrix} \mathbf{X}_\zeta^{n+1} \\ \mathbf{X}_D^{n+1} \end{pmatrix} = \begin{pmatrix} \mathbf{X}_\zeta^{n-1} + 2\Delta t\mathcal{C}_\tau \\ \mathbf{X}_D^{n-1} + 2\Delta t(\mathcal{D}_\tau + Fr^{-2}\mathbf{L} \cdot \mathbf{X}_h^{n-1}) \end{pmatrix}, \quad (\text{A.5})$$

where \mathbf{E} is the unit matrix and $\mathbf{C} = \mathbf{E} + 4\Delta t^2 Fr^{-2}\mathbf{L}$. Applying the inverse of the matrix to (A.5), we obtain the future values for vorticity and divergence. Future values of the surface elevation directly result from Eq. (A.3).

References

- Böning, C., 1986. On the influence of frictional parameterization in wind-driven ocean circulation models. *Dyn. Atmos. Oceans* 10, 63–92.
- Bourke, W., 1972. An efficient, one-level, primitive-equation spectral model. *Mon. Weather Rev.* 100, 683–689.
- Bourke, W., 1974. A multi-level spectral model. I. Formulation and hemispheric integrations. *Mon. Weather Rev.* 102, 687–701.
- Bryan, K., Cox, M.D., 1972. The circulation of the world ocean: a numerical study. Part I, a homogeneous model. *J. Phys. Oceanogr.* 2, 319–335.
- Cubasch, U., Hasselmann, K., Höck, H., Maier-Reimer, E., Mikolajewicz, U., Santer, B.D., Sausen, R., 1992. Time-dependent greenhouse warming computations with a coupled ocean-atmosphere model. *Clim. Dynam.* 8, 55–69.
- Fraedrich, K., Jansen, H., Kirk, E., Luksch, U., Lunkeit, F., 2005. The Planet Simulator: towards a user friendly model. *Meteorol. Zeitschrift* 14, 299–304.
- Gill, A.E., Clarke, A.J., 1974. Wind-induced upwelling, coastal currents and sea-level changes. *Deep-Sea Res.* 21, 325–345.
- Haidvogel, D.B., Robinson, A.R., Schulman, E.E., 1980. The accuracy, efficiency, and stability of three numerical models with application to open ocean problems. *J. Comput. Phys.* 34, 1–53.
- Haidvogel, D.B., Beckmann, A., 1999. *Numerical Ocean Circulation Modeling*. Imperial College Press, London. 325pp.
- Haltiner, G.J., Williams, R.T., 1980. *Numerical Prediction and Dynamic Meteorology*. John Wiley & Sons, New York. 477pp.
- Hasselmann, K., 1982. An ocean model for climate variability studies. *Prog. Oceanogr.* 11, 69–92.
- Held, I.M., Suarez, M.J., 1994. A proposal for the intercomparison of the dynamical cores of atmospheric general circulation models. *Bull. Amer. Meteor. Soc.* 75, 1825–1830.
- Hellerman, S., Rosenstein, M., 1983. Normal monthly wind stress over the world ocean with error estimates. *J. Phys. Oceanogr.* 13, 1093–1104.
- Hoskins, B.J., Simmons, A.J., 1975. A multi-layer spectral model and the semi-implicit method. *Quart. J. R. Meteor. Soc.* 101, 637–655.
- Kalnay, E., Kanamitsu, M., Baker, W., 1990. Global numerical weather prediction at the national meteorological center. *Bull. Amer. Meteor. Soc.* 71, 1410–1428.
- Kiehl, J.T., Hack, J.J., Bonan, G.B., Boville, B.A., Briegleb, B.P., Williamson, D.L., Rasch, P.J., 1996. Description of the NCAR Community Climate Model (CCM3), Technical Report NCAR/TN-420+STR, National Center for Atmospheric Research, Boulder, Colorado, 152 pp.
- Köhl, A., Dommenges, D., Ueyoshi, K., Stammer, D., 2006. The Global ECCO 1952 to 2001 ocean synthesis, Rep. 40, Natl. Oceanogr. Partnership Program Washington, DC, 43pp. (Available at http://www.ecco-group.org/ecco1/report/report_40.pdf).
- Köhl, A., Stammer, D., Cornuelle, B., 2007. Interannual to decadal changes in the ECCO global synthesis. *J. Phys. Oceanogr.* 37, 313–337.
- Lin, S.J., Rood, R.B., 1996. Multidimensional flux-form semi-Lagrangian transport schemes. *Mon. Weather Rev.* 124, 2046–2070.
- Leichtmann, D.L., Kagan, B.A., Oganessian, L.A., Piaskovsky, R.V., 1971. On the global circulation of an ocean with variable depth. *Proc. Acad. Sci., USSR* 198 (2), 333–336.
- Maier-Reimer, E., Mikolajewicz, U., Hasselmann, K., 1993. Mean circulation of the Hamburg LSG OGCM and its sensitivity to the thermohaline surface forcing. *J. Phys. Oceanogr.* 23, 731–757.
- Machenhauer, B., Rasmussen, E., 1972. On the integration of the spectral hydrodynamical equations by a transform method, Institute of Theoretical Meteorology, University Copenhagen, Report No. 3, 44pp.
- Matsuno, T., 1966. Quasi-geostrophic motions in the equatorial area. *J. Meteor. Soc. Japan* 44, 25–43.
- Mason, P.J., Sykes, R.I., 1978. A simple Cartesian model of boundary layer flow over topography. *J. Comput. Phys.* 28, 198–210.
- Munk, W.H., 1950. On the wind-driven ocean circulation. *J. Meteor.* 7, 79–93.
- Neelin, J.D., 1991. The slow sea surface temperature mode and the fast-wave limit: analytic theory for tropical interannual oscillations and experiments in a hybrid coupled model. *J. Atmos. Sci.* 48, 584–606.
- Olbers, D., Eden, C., 2003. A simplified general circulation model for a baroclinic ocean with topography. Part I: theory, waves, and wind-driven circulations. *J. Phys. Oceanogr.* 33, 2719–2737.
- Orszag, S.A., 1970. Transform method for the calculation of vector-coupled sums: application to the spectral form of the vorticity equation. *J. Atmos. Sci.* 27, 890–895.
- Philander, S., Yamagata, T., Pacanowski, R., 1984. Unstable air-sea interactions in the tropics. *J. Atmos. Sci.* 41, 604–613.
- Platzman, G.W., 1962. The analytical dynamics of the spectral vorticity equation. *J. Atmos. Sci.* 19, 313–328.
- Reinert, D., Wirth, V., Eichhorn, J., Panhans, W.-G., 2007. A new LES model for simulating air flow and warm clouds above highly complex terrain. Part I: the dry model. *Bound. Layer Meteor.* 125, 109–132.
- Roeckner, E., Bäuml, G., Bonaventura, L., Brokopf, R., Esch, M., Giorgetta, M., Hagemann, S., Kirchner, I., Kornblueh, L., Manzini, E., Rhodin, A., Schlese, U., Schulzweida, U., Tompkins, A., 2003. The Atmospheric General Circulation Model ECHAM 5. Part I: Model Description, MPI-Report 349, Max Planck Institute for Meteorology, Hamburg, 127pp.
- Sag, T.W., 1969. A numerical model for wind-driven circulation of the oceans of the world. *Phys. Fluids (Suppl. II)*, 177–183.
- Soares, J., Wainer, I., Wells, N.C., 1999. Reflection of equatorial Kelvin waves at eastern ocean boundaries Part I: hypothetical boundaries. *Ann. Geophys.* 17, 812–826.
- Stammer, D., Ueyoshi, K., Köhl, A., Large, W.G., Josey, S.A., Wunsch, C., 2004. Estimating air-sea fluxes of heat, freshwater, and momentum through global ocean data assimilation. *J. Geophys. Res.* 109, C05023. doi:10.1029/2003JC002082.
- Te Raa, L.A., Dijkstra, H.A., 2002. Instability of the thermohaline ocean circulation on interdecadal timescales. *J. Phys. Oceanogr.* 32, 138–160.
- Titov, V.V., Gonzalez, F.I., Bernard, E.N., Eble, M.C., Mofjeld, H.O., Newman, J.C., Venturato, A.J., 2005. Real-time tsunami forecasting: challenges and solutions. *Nat. Hazards* 35, 35–41.
- von Storch, J.S., Kharin, V.V., Cubasch, U., Hegerl, G.C., Schriever, D., von Storch, H., Zorita, E., 1997. A description of a 1260-year control integration with the coupled ECHAM1/LSG general circulation model. *J. Climate* 10, 1525–1543.
- Wunsch, C., Ferrari, R., 2004. Vertical mixing, energy, and the general circulation of the oceans. *Annu. Rev. Fluid Mech.* 36, 281–314.